Accepted Manuscript
Version of Record at: https://doi.org/10.1002/pen.26700

A Novel Digital Lifecycle (DLC) for Material-Process-Microstructure-Performance (MP2) relationships of Thermoplastic Olefins Foams Manufactured via Super Critical Fluid (ScF) Assisted Foam Injection Molding

Sai Aditya Pradeep [1], Amit M Deshpande [1,2], Pierre-Yves Lavertu [1,3], Ting Zheng [4], Veera Aditya Yerra [4], Yiro Shimabukuro [5], Gang Li [6], Srikanth Pilla [,1,2,3,7]*

[1]Center for Composite Materials, University of Delaware, Newark, DE-19716
[2]Department of Mechanical Engineering, University of Delaware, Newark, DE-19716
[3]Department of Materials Science and Engineering, University of Delaware, Newark, DE-19716
[4]Department of Automotive Engineering, Clemson University, Greenville, SC-29607
[5]Polymers Center for Excellence, Charlotte, NC-28262
[6]Department of Mechanical Engineering, Clemson University, Clemson, SC- 29631
[7]Department of Chemical and Biomolecular Engineering, University of Delaware, Newark, DE-19716
*Corresponding author: spilla@udel.edu; Ph: 302-831-3182

Abstract: This research significantly enhances the applicability of Thermoplastic Olefins (TPOs) in the automotive industry using Supercritical N_2 as a physical foaming agent, effectively addressing the limitations of traditional chemical agents. It merges experimental results with simulations to establish detailed material-process-microstructure-performance (MP2) relationships, targeting 5-20% weight reductions. This innovative approach labelled Digital Lifecycle (DLC) helps accurately predict tensile, flexural, and impact properties based on the foam microstructure, along with experimentally demonstrating improved paintability. The study combines process simulations with finite element models to develop a comprehensive digital model for accurately predicting mechanical properties. Our findings demonstrate a strong correlation between simulated and experimental data, with about a 5% error across various weight reduction targets, marking significant improvements over existing analytical models. This research highlights the efficacy of physical foaming agents in TPO enhancement and emphasizes the importance of integrating experimental and simulation methods capturing the underlying foaming mechanism to establish material-process-microstructure-performance (MP2) relationships.

Highlights:

- Establishes a material-process-microstructure-performance (MP2) for TPO Foams
- Sustainable produces TPO foams using supercritical N_2 with 20% lightweighting
- Shows enhanced paintability for TPO foam improved surface aesthetics
- Digital Lifecycle (DLC) that predicts both foam microstructure and properties
- DLC maps process effects & microstructure onto FEA mesh for precise prediction

Accepted Manuscript
Version of Record at: https://doi.org/10.1002/pen.26700

Keywords: Thermoplastic Olefins, Thermoplastic foams, Microcellular foaming, Microstructure-process-property relationships (MP2), Automotive Lightweighting, Digital Lifecycle (DLC), Integrated Computational Materials Engineering (ICME)

Introduction

Given that the global transportation industry is the second highest contributor to climate change, there has been a concerted effort to spearhead research in economic lightweighting technologies; notably, every 10 % reduction in weight leads to a 6 – 8% improvement in fuel efficiency [1]. A direct consequence of this has been the increasing adoption of polymers in automobiles, which went from 20 lbs. in 1960 to 257 lbs. in 2010 [2]. Among the different plastics used, Thermoplastic Olefins (TPOs) have, in recent years, carved out a niche in the automotive industry due to advantages like increased impact resistance, lower production costs, short production times, and improved fuel efficiency on account of lower densities [3,4]. TPOs have been successfully used in interior and exterior automotive applications such as bumpers and fascias, trims, cladding, and wire insulation [4–6]. Logically, adopting TPO foams via the conventional chemical or new physical blowing agents would largely benefit the Automotive sector, given the need to drive down weight and increase efficiency [7,8].

However, conventional TPO foams have not seen widespread adoption in the automotive industry. In general, TPO foams can be manufactured via 2 different approaches using chemical or physical foaming agents in existing manufacturing processes like injection molding. Currently, TPO foams are the standard choice produced using chemical foaming agents. This is primarily due to their low initial costs and ability to yield a well-molded color appearance. However, there are certain challenges associated with this method. For instance, unpredictable foaming can occur in different cross sections, thermal stability can decrease, and residual foaming agent migration may occur due to weather changes. These factors can lead to pitting in class A painted surfaces [9,10]. One of the earliest papers in this area was by Guo et al. [11] investigated the effects of chemical foaming agent concentration, injection parameters, and melt rheology on the occurrence of surface defects. Subsequently, Santoni et al. [12] fabricated a blend of TPO and maleic anhydride-modified PP to achieve a 20 % weight reduction using an azodicarbonamide foaming agent wherein the addition of PP-g MA improved the good surface quality. Lastly, Peyda et al. [13] used microwave radiation and azodicarbonamide as CFA in a PP/EPDM system with PP-g-MA to achieve uniform void size and distribution without surface appearance data.

An alternative method for manufacturing TPO foams involves using physical foaming agents, such as supercritical nitrogen or carbon dioxide. This method is considered more sustainable and yields consistent, small micron-sized voids. However, despite these benefits, it has yet to be widely adopted by the industry due to higher initial costs (paid back relatively quickly [14]) and the potential for splay marks on the surface. These marks would not meet the molded-in color appearance requirements for most OEMs. Another important challenge of foaming TPOs via supercritical gases, particularly nitrogen, is the lower solubility of supercritical N_2 in PP and the

Accepted Manuscript
Version of Record at: https://doi.org/10.1002/pen.26700

uneven distribution of the Ethylene-propylene-copolymer phase in PP [15]. The earliest research in this area was by Wong et al. [16] studied the effect of different processing parameters on the mechanical properties of TPO foams and proposed constitutive models to help material-process-microstructure-performance (MP2) relationships. Consequently, Kim et al. [17] studied the effect of different talc contents while using N_2 as the blowing agent and using a batch foaming simulation system which typically does not account for the flow field and thus falls short of accurate prediction of microstructure [13]**.** Lastly, Kim et al. [18] followed this up by investigating the effect of elastomer dispersion on TPO foamability by preparing different blend morphologies controlled by the viscosity ratio between the blending components. None of these studies listed above measured instrumented impact properties of TPO foams or investigated the effect of accelerated aging on molded color or painted plaques.

To the authors' best knowledge, there is insufficient data or research in three critical areas that prevent the widespread adoption of physically foamed TPOs – (i) measurement of instrumented impact properties of TPO foams at different weight reduction percentages (ii) investigation of the effect of accelerated aging on molded-in color or painted plaques (iii) creation of a novel simulation pathway for TPO foams that combines rheological and bubble growth models to predict cell microstructure and uses mean-field homogenization and FEA models to map residual stresses and microstructure, resulting in accurate mechanical property predictions.

All three areas are crucial in evaluating these TPO foams and play a role in their adoption by automotive OEMs. Lastly, from a simulation pathway perspective, two key areas are crucial to creating a Digital Lifecycle pathway and their coupling. The first is the ability to predict foam microstructure that incorporates coupling of rheological and nucleation models that can reliably predict cell size and density. The only work in this regard was by Xi et al. [19] used a modified cross-model to describe the rheological properties of generic PP and nucleation models in Moldex 3D to predict foam morphology, and Oikonomou et al. [20] used a modified Han and Yoo model with generic rheological properties of PP to help predict the microstate of special pull and foam injection molding techniques. The second is mapping the foam microstructure to predict their mechanical response. Almost all the current direct and constitutive modeling approaches for foams [21–24] use experimental inputs of foam microstructure in their models to predict mechanical properties (shown in Figure 11). No coupling is established between manufacturing-based models or simulations that predict microstructure and mechanical models that take these inputs to predict mechanical properties.

This paper addresses the triumvirate of research gaps listed above while giving a holistic perspective of rich experimental results and details of a coupled simulation pathway adopted to predict foam microstructure and mechanical properties.

Materials and Methods

A polypropylene and ethylene propylene copolymer TPO was graciously supplied from advanced composites (OH, USA) with a specific gravity of 0.94 and melt flow index of 31 g/10 min.

Accepted Manuscript
Version of Record at: https://doi.org/10.1002/pen.26700

Commercial grade nitrogen was sourced from Airgas (Greenville, SC, USA), and used as the blowing agent for Super Critical Fluid (ScF-) assisted injection molding.

The TPO pellets were dried at 80 °C for 8 h before injection molding (IM). Conventional and ScF IM were carried out using an injection molding machine (Engel Victory 30, York, PA, USA) equipped with an integrated Trexel ScF Dosing system (Willimington, MA, USA). Injection molding optimization trials consisting of 3 studies (Figure 1) were conducted to optimize the microstructure and obtain microcellular morphology and are shown below:

$$ScF\ N_2\ wt.\ \% = \frac{\text{Gas Flow Rate} * \text{ Gas Dosage Time } * 27.8}{Shot\ Weight} \qquad (1)$$

1. Study I :- Reducing shot volume at constant ScF N_2 wt. %: 3 %, 8 %, 10 %, 17 % 20 %

2. Study II :- Varying low gas dosage, processing temperature, constant shot volume.
   Low ScF N_2 wt. % : 0.19

3. Study III :- Varying high gas dosage, processing temperature, injection parameter, and constant shot volume Hight ScF N_2 wt. % : 0.39

The studies revealed that higher melt temperatures & ScF dosage with lower injection speed were crucial in improving ScF N_2 solubility and obtaining microcellular cellular morphology. Details of this optimization were published in our SPE ANTEC Technical Paper 2019 [25].

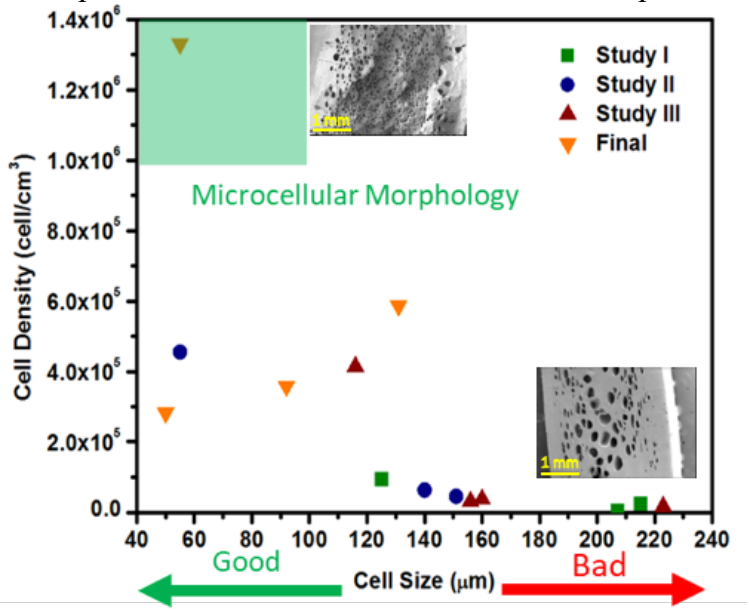

Figure 1. Details the cell size and densities achieved by varying processing conditions based on our previous studies [25]

Accepted Manuscript
Version of Record at: https://doi.org/10.1002/pen.26700

The finalized list of process conditions for the foams obtained in this study is shown in Table 1.

Table 1. Process Conditions used for Foam Injection Molding

Parameter	Solid Molding	FIM 5 % wt reduction	FIM 10 % wt reduction	FIM 15 % wt reduction	FIM 20 % wt reduction
Back pressure (MPa)	9.9				
Melt temperatures (°C)	240 | 240 | 230 | 220 | 180				
Injection pressure (bar)	130	140	140	140	140
Injection speed (cm3/s)	23.1	60	60	60	60
Holding pressure (bar)	150	NA			
Holding time (s)	10	NA			
Cooling time (s)	60				
ScF N_2 dosage (wt %)	NA	0.36	0.38	0.40	0.43

Scanning Electron Microscopy

Scanning electron microscopy (Hitachi, S 4800, Tokyo, Japan) was used to study the cell size and density of the foamed samples. Samples were cryogenically cracked in the center of the plaques after immersing them in liquid nitrogen for 30 minutes using a vice and rubber mallet to preserve the internal cellular structure. Before imaging, these samples were coated for 2 mins with platinum using a Hummer 6.2 sputtering system. Cell size and density of these foams were characterized from these SEM images using commercial image processing software, Image J. The cell density (N) was calculated using the following equation [26]:

$$N = \left(\frac{n}{A}\right)^{\frac{3}{2}} \quad (2)$$

Where N is the number of cells, L is the linear length of the area, and M is a unit conversion resulting in the number of cells per cm^3.

Differential Scanning Calorimetry

A differential scanning calorimeter (TA Instruments, Q2000, New Castle, DE, USA) was used to study the crystallization behavior of all solid and foamed samples. About 3 - 5 mg of sample was taken in hermetically sealed aluminum pans, nitrogen was used at 20ml/min. Samples were subjected to heating/cooling/heating cycles at 5 °C /min, beginning with heating from −100 to 200 °C (to remove any thermal history from processing).

Accepted Manuscript
Version of Record at: https://doi.org/10.1002/pen.26700

$$X_c\ (\%\ crystallinity) = \frac{\Delta H_m - \Delta H_{cc}}{\Delta H^0} \times \frac{100}{W} \quad (3)$$

Thermal Mechanical Analysis

A thermal mechanical analyzer (TA Instruments, Q2000, New Castle, DE, USA) was used to study the dimension changes as a function of the temperature of all solid and foamed samples. Samples of dimensions 1 mm x 1 mm were cut with parallel faces, and experiments were performed in expansion probe mode. Samples were subjected to a heating cycle from -30 °C to 105 °C using a ramp rate of 5 °C /min.

Tensile Tests

Tensile tests were performed on a universal testing machine (Instron, 5598, Norwood, MA, USA) to study the ultimate tensile strength and Youngs modulus. At least 5 samples were punched out of the injection molded plaques using a die following ASTM D 638.

Three-point flexural tests

Three-point flexural tests were performed on a universal testing machine (Instron, 5892, Norwood, MA, USA) having a 10 kN load cell to study flexural strength and modulus. A crosshead speed of 12.8 mm/min was used with a support span of 48 mm. At least 3 samples were tested after punched out of injection molded plaques using a die following ASTM D790.

Instrumented impact tests

Instrumented impact tests were conducted on a drop tower impact tester (Instron, 9450, Norwood, MA, USA) to study force vs. time response. An impact velocity and height of 1.98 m/s and 202 mm was used. At least 3 samples were tested following ASTM D 3763.

Accelerated Ageing tests

Accelerated Ageing or weathering tests were carried out on a weathering meter (SUGA, SWOM, Tokyo, Japan), molded in color, and painted plaque. A confidential Honda standard was used to conduct these tests based on internal know-how and anticipated vehicle environment. A BYK spectrophotometer was used to measure gloss retention and ΔE on molded-in color and painted samples (3 speciemens per sample) before and after the test.

Surface Roughness tests

Accepted Manuscript
Version of Record at: https://doi.org/10.1002/pen.26700

Surface roughness tests were conducted on an optical surface profiler (Zygo, NewView 7200, Berwyn, PA, USA) on molded-in-color specimens. A scan size of 0.71 mm x 0.53 mm was scanned, and arithmetical mean height (Ra), Maximum profile valley depth (Pv), 2D image, and 3D model of the surface were generated.

Capillary Rheometer tests

Viscosity, Thermal conductivity (TC), and pressure-volume-temperature (PVT) measurements were performed on a Gottfert Capillary Rheometer RG 20. Shear viscosity experiments were performed using a 30/1 L/D die with a shear sweep from 10-10,000 s^{-1} (half-decade increments) at 200 °C , 220 °C , and 240 °C Apparent shear values were corrected using the Rabinowitsch-Weissenberg equation to correct for shear rates close to the barrel wall. TC was performed using the Goettfert TC add-on package using a 24 V powered linear probe. PVT was conducted with the Goettfert RG PVT add-on package with a Julabo heat exchanger.

Process Simulations: Conventional and Foam Injection Molding

The conventional and foam injection molding processes were simulated via the CAE-based software Moldex 3D. A CAD model of the cavity was imported and important injection molding attributes such as gate type, gate dimensions, melt inlet, plaque dimensions, mold base dimensions, and cooling channels were modeled and meshed in Moldex 3D. Specifically, the entire model was meshed using the solid Boundary Layer Meshing (BLM) method. BLM is one of the most suitable meshing approaches for flow analysis in enclosed cavities, such as plastic melt flow during injection molding. It accurately captures the viscoplastic shear effects representative of the non-Newtonian fluid flow of plastic at the interacting surfaces of the cavity using fine mesh layers. However, beyond a certain point within the plastic melt, the bulk behavior is captured in a more computationally efficient manner using a relatively coarse tetrahedral mesh. During the meshing process, the solid part (plaque) is divided into three sections, where the top and bottom sections close to the skin region are meshed using Tetrahedral elements. In contrast, the center region is meshed using Prism elements. This layout of different types of elements helps capture more accurate simulation results while being computationally less challenging.

Once the initial setup was done, a custom rheological data card was developed that tries to capture the properties using the listed experiments shown in Table 2.

Table 2 Properties, experiments, and models used to create a process data card.

S.no	Property	Experimental Condition
1	Shear Viscosity	Shear rate: 0.001 ~ 10 sec^{-1} at 180, 205 and 230 °C (ASTM D4440)
2	Pressure-Volume-Temperature (PVT)	Full temperature run (10 to 300 °C) at 0, 50, 100, 150 and 200 MPa (ISO 17744)
3	Thermal conductivity	Measured at 40, 100, 150, 200, 250 and 300 °C (ASTM D 5930)

Accepted Manuscript
Version of Record at: https://doi.org/10.1002/pen.26700

4	Heat Capacity	Heat past Tm and cool to 40 °C at a constant rate of 20 °C (ASTM E1269)
5	Coefficient of Thermal Expansion	ASTM E831
6	Crystallization Kinetics	Heat past Tm and cooled at 5, 10, 15, 20, 40 and 60 °C /min
7	Fluid Viscoelasticity	0.1~400 rad/s at 130, 140, 150, 160,170, 190, 210 °C (ASTM D4065)
8	Structural Viscoelasticity	0.1~100 Hz at 40, 60, 80, 100, 120, 140, 150 and 160 °C in Flex loading (ASTM D5023)

This study focused on two main aspects to forge a Digital Lifecycle (DLC) pathway which make this pathway superior to other approaches. Firstly, it emphasizes the prediction of foam microstructure through the integration of rheological and nucleation models, which are vital for accurately estimating cell size and density. Secondly, the research underlines the importance of translating the foam microstructure into a mechanical response prediction. While most current models depend on empirical foam structure data to predict mechanical characteristics, the paper identifies a gap in linking simulation-derived microstructural predictions with mechanical property predictions, an area that remains unaddressed in existing literature. The major advantages of this include reducing time and cost by replacing extensive physical experiments to investigate microstructure-process-property (MP2) relationships with efficient simulations. This method accelerates research, is less expensive, and allows for a broader exploration of process variables, enhancing the development and optimization of materials and processes.

Results & Discussion

Cell Structure

Microstructural characterization of the TPO foams that were lightweighted by 5, 10, 15, and 20 wt% were carried out using SEM. Figure 2 shows how cell size and density vary as a function of weight reduction. The average cell size consistently increased as a function of higher ScF N_2 wt % and higher lightweighting with 15 and 20% samples exhibiting large and non-uniform cell distributions [27]. Cell densities improved from 5 to 10 % but decreased for 15 and 20 % lightweighting samples. This is a common trend observed in weight reductions higher than 10 % (i.e., lower shot volumes) with higher dosages of ScF wt % that often lead to increased cell coalescences, thereby increasing cell diameter and lowering cell densities [28]. Additionally, from a theoretical perspective, the trend that cell density increased first and then decreased is associated with the cell nucleation-controlled and cell growth/coalesce-controlled process. In the former step, the higher weight reduction (from 5% to 10%, achieved by lowering the shot volume) gave more space for melt to expand, leading to a higher rate of depression (ΔP) and, accordingly lower energy barrier for nucleation (ΔG), smaller critical nuclei size (Rc) and eventually higher nuclei density

Accepted Manuscript
Version of Record at: https://doi.org/10.1002/pen.26700

[29]. However, when the weight reduction further increased, bubbles expanded to their full potential with less mold cavity restriction followed by the cell break and coalesce. Together with the delusion of the cell density during the expansion, the cell coalesces, resulting in the decrease in cell density, as observed in Figure 2.

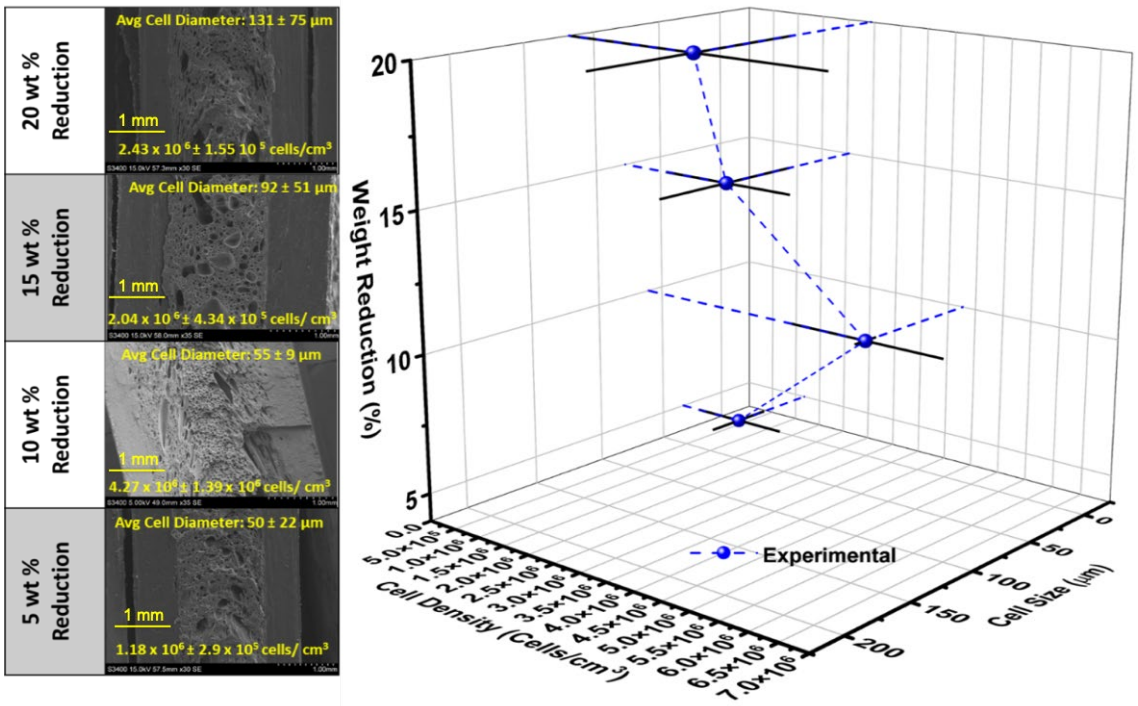

Figure 2. SEM images and plots of cell size vs. density vs. weight reduction of sample images after cryogenically cracking.

Thermal Properties

The thermal properties, particularly the crystallinity and dimension change of the solid and foamed, were characterized using DSC and TMA and are shown in Figure 3a and Figure 3b. When comparing crystallinity, all the foamed samples exhibited higher % crystallinity than the corresponding solid samples. This increase could be due to the extensional flow of the ScF N_2 affecting the orientation of the polymer molecules around the cell walls, leading to strain-induced crystallization; such behavior was first reported by Ameli et al. [30].

The change in dimension with respect to temperature, specifically from -30 to 105 °C , is extremely important to qualify materials in the automotive industry. The dimension change as a function of temperature was measured and compared to an Aluminum 6061 reference. Among the TPO samples, the solid, the 5%, and the 10% weight reduction samples showed a linear trend in dimension change, with the solid sample showing the highest dimension change when compared to the foamed TPO specimens. Interestingly, a lower dimension change over the temperature range 45 °C to 105 °C was reported by 10% and 15% lightweighting samples compared to solid and

Accepted Manuscript
Version of Record at: https://doi.org/10.1002/pen.26700

20% foamed samples. This knowledge that the CTE of foams is lesser than their solid counterparts can help tool and part designers assign accurate tolerances and better integrate foamed parts in any assembly of their choice, thereby increasing their overall adoption by industry [31]. To the best of our knowledge, dimensional changes of polymer foams compared to parent solid material over a temperature range have not been reported in the literature.

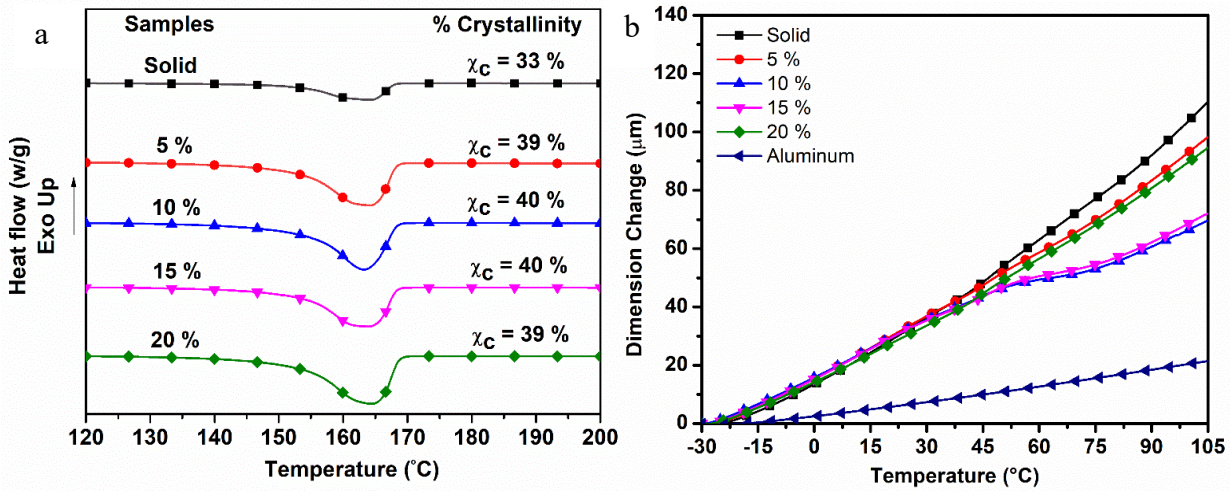

Figure 3. a) Differential Scanning Calorimetry curves (Second Heating) of solid and foamed samples (Avg of 3 samples) b) TMA of solid and foamed samples (Avg of 3 samples)

Mechanical Properties

The average stress-strain response and statistical analysis of Young's Modulus and ultimate tensile strength of the solid and foamed TPO sample are shown in Figure 4a and Figure 4b, respectively. The modulus and ultimate tensile strength show a linear or stepwise decline that is statistically significant. Young's Modulus or stiffness was reduced by 20 % for 5 % weight reduction samples and 23%, 34%, and 35% for 10 wt %, 15 wt %, and 20% weight reductions, respectively, which is generally attributed to the reduction in overall material per unit volume of the foam [16]. Wong et al.[16] also observed a linear decline in Young's Modulus and ultimate tensile strength as a function of weight reduction in TPO foams using supercritical N_2 as a foaming agent. Interestingly the ultimate tensile strength only reduced by ~ 10% for 5% weight reduction and 18%, 23% and 32% for 10 wt%, 15 wt%, and 20 wt% reductions, respectively. There could be two reasons for the relatively smaller decline in strength compared to modulus. One proposed by Wong et al. [16] and the other by Sun et al. [32]. The first proposed by Wong et al. [16] is that a foam with a well-distributed cellular structure improves mechanical strength retention. The second proposed by Sun et al. [32] that is postulated specifically for microstructures consisting of microcellular voids (voids in a PP matrix) and a sub-micron immiscible secondary phase (like EPDM). Tensile loading of this specific microstructure leads to the cavitation of this secondary phase facilitating an interconnection of microcellular voids for channels leading to the stretched component forming fibrils. This change in structure transforms the fracture mechanism from crack propagation across

Accepted Manuscript
Version of Record at: https://doi.org/10.1002/pen.26700

the polymer matrix into shear, yielding a bundle of fibrils, thereby improving toughness and strength retention.

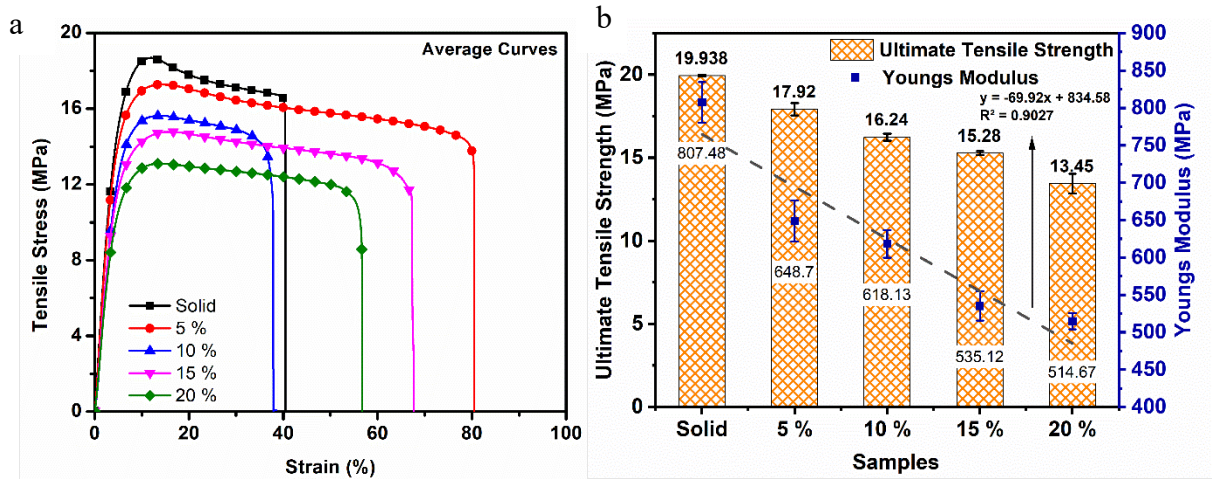

Figure 4. a) Plot of average tensile stress-strain curves b) Statistical analysis of ultimate tensile strength and Young's modulus of solid and foamed samples.

The average flexural stress vs. strain response and statistical analysis of flexural strength and modulus are shown in Figure 5a and Figure 5b. The flexural strength showed a near-linear decline with an increase in weight reduction. Specifically, the flexural strength was reduced by 7% for 5 wt% reductions and 13%, 21%, and 35% for 10 wt%, 15 wt%, and 20 wt% reductions compared to solid specimens. The Flexural modulus, on the other hand, reduced linearly from 5 wt% to 15 wt% reduction and plateaued at 20 wt% reduction. The flexural modulus was reduced by 5% for the 5% wt reduction and by 18%, 26%, and 24% for the 10 wt%, 15 wt%, and 20 wt% reduction compared to solid specimens. No literature exists on the flexural response of TPO foams in particular. Still, at least a few experimental results exist on LDPE foams [33] and theoretical models that highlight a similar decline in flexural modulus with decreasing density reduction [34], as shown later. More specifically, these two models were compared with experimental flexural results of LDPE foams fabricated by Yang el al. [33] with densities ranging from 0.791 to 0.859 g/cm^3. The experimental results from the literature study show a statistical decline in flexural modulus with decreasing density. The Lee and Westmann model [35] was able to accurately predict flexural modulus for smaller densities (0.791 to 0.845 g/cm^3) quite well, and Ogorkiewicz and Sayigh model [36] was found to be accurate for larger densities (>0.859 g/cm^3).

Accepted Manuscript
Version of Record at: https://doi.org/10.1002/pen.26700

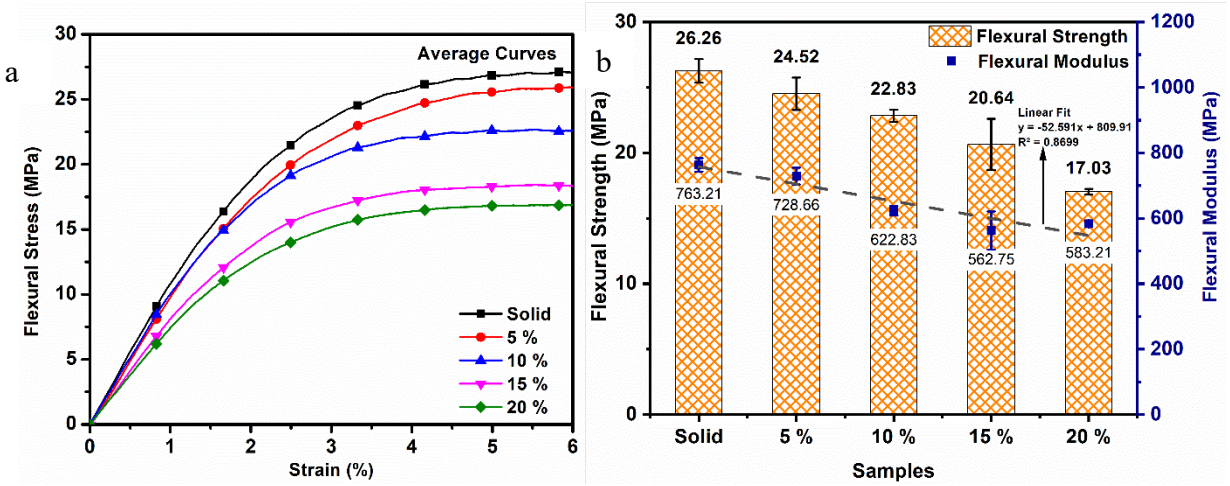

Figure 5. a) Plot of average flexural stress-strain curves b) Statistical analysis of flexural strength and Modulus of solid and foamed samples.

The average force vs. time response and statistical analysis of the instrumented impact tests on solid and foamed TPO samples are shown in Figure 6a and Figure 6b, respectively. The peak force and energy show a linear decline till 15% weight reduction and plateau at 15 and 20% weight reduction with no significant statistical difference in properties between 15 and 20 % weight reduction. Specifically, the peak force was reduced by 15% for 5 wt% reductions and 26%, 42%, and 44% for 10 wt%. When compared to solid specimens, 15 wt% and 20 wt% reduction. Similarly, peak energy was reduced by 2% for 5 wt % reduction and 33%, 55% and 55% for 10 wt%. When compared to solid specimens, 15 wt% and 20 wt% reduction. While no data for TPO foams undergoing dynamic impact or Gardner impact tests exists in the literature, Kumar et al. [37] and Burea et al. [38] did test Crystallizable Poly Ethylene Terephthalate (CPET) and Polystrene (PS) foams at various relative densities. Kumar et al. [37] observed a decline in impact energy as a function of density reduction at room temperature, -17.8 °C, -28.9 °C, and - 40 °C while noting that increased crystallinity at the same density reductions exhibited better impact response. Burea et al. [38] also broadly observed peak force and total load decreased with increasing density reduction, more specifically foams, with they identified a key factor labeled microstructural parameter (density/cell diameter), which proved to be a good predictor that accounted for the influence of cell size. One hypothesis for both trends is that smaller, well-dispersed cells can dissipate energy more effectively while larger cells behave as obstacles to crack propagation through the matrix.

Accepted Manuscript
Version of Record at: https://doi.org/10.1002/pen.26700

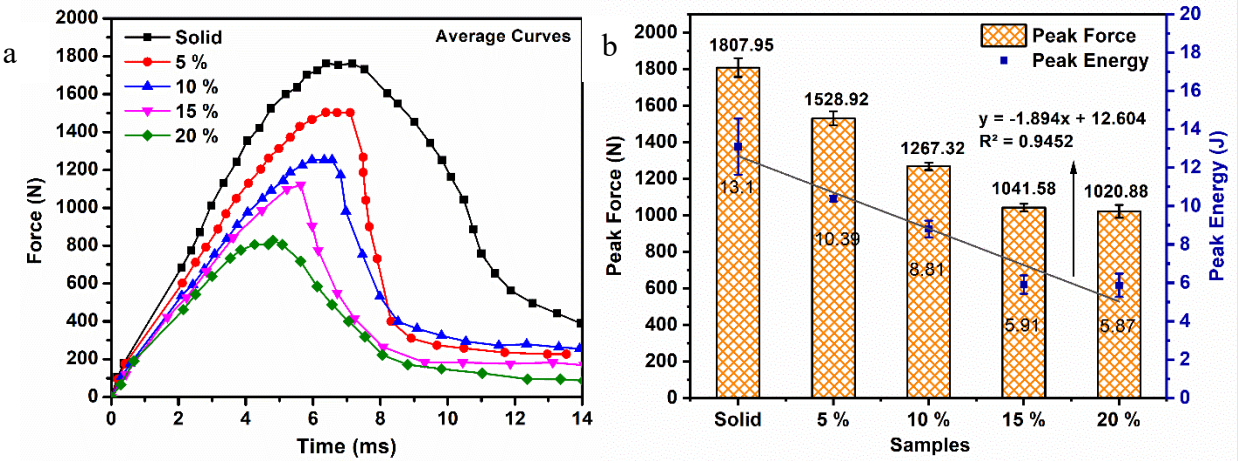

Figure 6. a) Plot of average instrumented impact response of solid and foamed samples b) Peak force and peak energy response of solid and foamed specimens

Molded in Color and Paintability

The delta E (ΔE) results of molded in color solid and foamed TPO plaques after accelerated ageing tests are shown in Figure 7a, while the gloss retention of solid and foamed TPO plaques which have been painted is shown in Figure 7b. The color accuracy (ΔE) is a standard measurement that numerically quantifies the difference or distance between 2 colors in colorspace, in our case, the difference of the solid plaque and the foamed plaques. Typically, a ΔE below 1 is imperceptible to the human eye, ΔE between 1 – 2 is perceptible through close observation and ΔE between 2 – 10 is perceptible at first glance. In our study ΔE of the foamed TPO plaques with respect to solid generally showed a ΔE of 9.9 and higher making it a very perceptible color difference with ΔE generally increasing with increasing weight reduction.

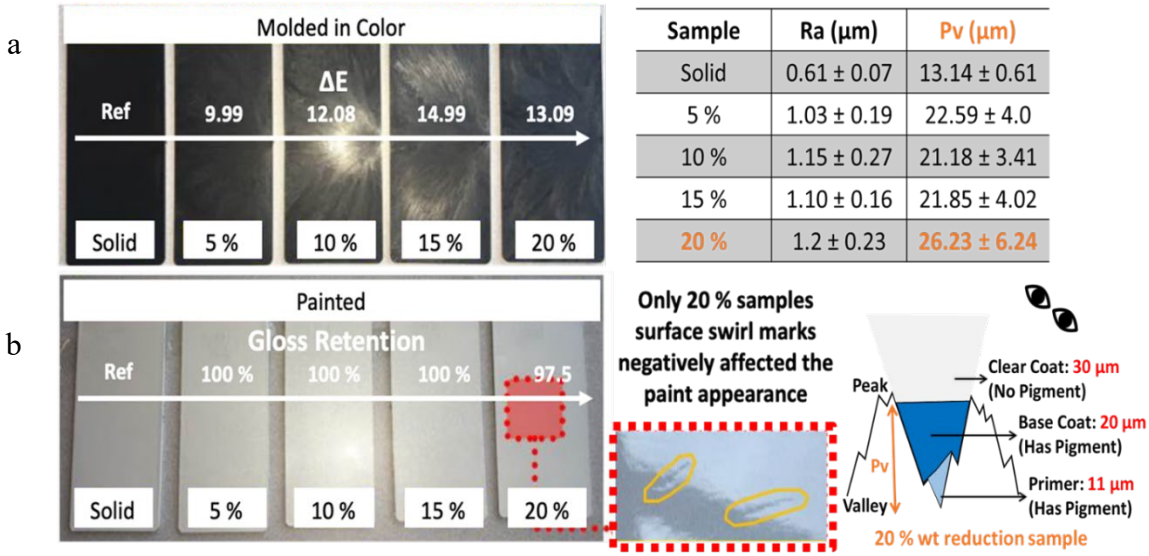

Sample	Ra (µm)	Pv (µm)
Solid	0.61 ± 0.07	13.14 ± 0.61
5 %	1.03 ± 0.19	22.59 ± 4.0
10 %	1.15 ± 0.27	21.18 ± 3.41
15 %	1.10 ± 0.16	21.85 ± 4.02
20 %	1.2 ± 0.23	26.23 ± 6.24

Figure 7. Visual comparison of a) Molded in Color and b)Painted Plaques that show changes in color space and Gloss retention as a function of lightweighting using a spectrophotometer.

Accepted Manuscript
Version of Record at: https://doi.org/10.1002/pen.26700

Although no literature specifically exists comparing the ΔE of solid and foamed specimens, there have been several studies that have reported these white splay marks. Most studies agree that the white splay marks are caused when bubbles forming at the advancing melt front are first stretched by fountain flow behavior toward the mold surface and later dragged against the mold wall [39]. Although there is a great body of research that tries to solve the issue of splay marks, almost all of them use additional costly equipment leading to difficulties in applying this technology in the industrial context like the use of gas counter pressure [40] and mold heating [41]. A study by Lee et al. [27] is the only research carried in literature that tries to improve the surface quality by controlling the cell nucleation rate without using any additional equipment. This work focused on identifying the degree of supersaturation (4) which represents a controllable factor that can help in increasing or decreasing the activation energy for nucleation (ΔG^{**}) [27]

$$\Delta G^{**} = \frac{16\pi\gamma^3}{3\left(kT\rho_1 ln\frac{P_r}{P_\infty}\right)} \quad (4)$$

Where γ is the surface energy of the bubble interface, k is Boltzmann constant, ρ is density, P_∞ is Pressure of the saturated vapor, and P_r - Pressure of the supersaturated solution in the sample.
Lee et al. [27] postulated that by reducing the degree of supersaturation $\left(\frac{P_r}{P_\infty}\right)$ the activation energy required for cell nucleation would increase. This, in turn, impedes cell nucleation during the filling stage, thus preventing the formation of bubbles on the melt front of the polymer gas solution resulting in swirl-free IM parts. The authors identified 0.175 wt % ScF as the threshold to achieve this swirl-free finish at an 8 wt % reduction level for polypropylene (PP). For our TPO (~ 80 % PP) material system using a ScF wt % of 0.38 was crucial in obtaining the least cell diameter with minimal standard deviation (61 µm ± 10) to maximize mechanical property retention but conversely led to the prevalence of white splay marks in MIC foamed specimens.

A separate set of solid and foamed TPO plaques were painted using OEM paint lines and proprietary paint composition and subjected to OEM-specified accelerated ageing tests. In contrast, these painted plaques showed a 100 % gloss retention for TPO foamed specimens up to a 15 wt% reduction. There was a 2.5% decrease in gloss retention for the 20 wt% reduction. One possible explanation for this reduction could be gleaned by comparing the surface roughness on the MIC plaques (specifically the height between peak and valley: Py) and the thickness of the primer and base coat (OEM spec). Based on internal surface roughness measurement using an optical profilometer, we know the distance between the peak and valley Py is ~ 26 µm. The paint on these plaques consists of a primer and base coat with a total height of 31 µm. Since the primer and base coat are the only components of the paint that have a pigment. Therefore, we can see how it would fail to cover up the surface roughness, specifically in the case of 20 wt % and not the other samples.

Accepted Manuscript
Version of Record at: https://doi.org/10.1002/pen.26700

Modelling

Digital Lifecycle (DLC) Pathway

A material's behavior generally depends on its microstructure, which is often impacted by the manufacturing process. Linking the material mechanical behavior to microstructure characteristics becomes very valuable as it allows a seamless connection between the manufacturing process and the mechanical behavior of a given part. Most studies focus on the mechanical material model alone, which has limited applications and reaches its full potential when tied to process simulation outputs. As mentioned before, no existing studies in literature couple manufacturing-based models that predict microstructure to mechanical models that take these inputs to predict mechanical properties. The general framework for the proposed DLC pathway for foams can be broken down into five steps: 1) Process data card generation (Table 3) for injection molding and mechanical analysis. 2) Injection molding simulation and experimental validation by comparing part weight and density 3) Foam injection molding simulation and obtaining correction factor for nucleation by comparing it with 1 experimental result. 4) Mapping of foam microstructure and flow-induced residual stress effects. 5) Evaluating the simulating tensile and flexural response with experimental trials.

Table 3 Properties, experiments, and models used to create a process data card.

S.no	Property	Model used
1	Shear Viscosity	Modified cross model
2	Pressure-Volume-Temperature (PVT)	Modified Tait model
3	Thermal conductivity	CAE K model
4	Heat Capacity	CAE Cp model
5	Coefficient of Thermal Expansion	-
6	Crystallization Kinetics	Nakamura model
7	Fluid Viscoelasticity	Giesekus model
8	Structural Viscoelasticity	Time temperature superposition principle to generate master curve

Conventional or solid injection molding simulations were performed following input conditions that matched with experimental conditions. Foam injection molding simulations, especially in the context of ScF foam injection molding are based on three bubble growth models - Han and Yoo, Shafi and Pavyar [42] and one nucleation model.

Han and Yoo:

Accepted Manuscript
Version of Record at: https://doi.org/10.1002/pen.26700

$$\frac{d}{dt}(P_D R^3) = \frac{6D(\Re_g T)(C_\infty - C_R)R}{-1 + \left\{1 + \frac{2\,/\,R^3}{\Re_g T}\left(\frac{P_D R^3 - P_{D0}R_0^3}{C\infty - C_R}\right)\right\}^{1/2}} \quad (5)$$

Pavyar:

$$\frac{d}{dt}(P_D R^3) = 3D(\Re_g T)(C_\infty - C_R)R \text{ x } \left[1 + \frac{1}{-1+\left\{1+\frac{1/R^3}{\Re_g T}\left(\frac{P_D R^3 - P_{D0}R_0^3}{C\infty - C_R}\right)\right\}^{1/2}}\right] \quad (6)$$

Shafi:

$$\frac{d}{dt}(P_D R^3) = \frac{36}{5} \cdot \frac{R^4(\Re_g T)^2 (C\infty - C_R)^2}{p_D R^3 - p_{D0}R_0^3} \quad (7)$$

where, D is the diffusion coefficient of gas in polymer, and k_H is the amount of gas dissolve in polymer under applied pressure.

While the user needs to experiment with the choice of bubble growth model, the nucleation model has two fitting factors (F and f_o) that can be used to properly fit or match the results of one experimental condition, 15 wt% weight reduction. We arrived at a value of F = 0.001 and f_o = 5.00E-24 to obtain a close correlation with our one experimental result for 15 wt % reduction. The same fitting factors were used for the remaining weight reduction levels: 5, 10, and 20%. In all these cases, only the gas weight percentage was varied while keeping all the other input parameters constant, as shown in Table 4.

Table 4. Input parameter for conventional and foam injection molding simulations

Input Parameters	**Solid**	**5%**	**10%**	**15%**	**20%**
Max Injection Pressure (MPa)		140			
Max Packing Pressure (MPa)		15			
Filling Time (s)		0.4	1.26	1.26	1.26
Packing Time (s)		0.1			
Melt Temperature (°C)		220			
Mold Temperature (°C)		40			
Shot Weight Control (VP Switch)		100	99	95	94
Initial Gas Concentration (wt%)		0.36	0.38	0.4	0.43
Cooling Time (s)		70			

Accepted Manuscript
Version of Record at: https://doi.org/10.1002/pen.26700

Eject Temperature (°C)		114
Bubble Growth Model		Han and Yoo
Correction factor (f_o)		5.00E-24
Correction Factor (F)		0.001
Threshold of Bubble (J_t)		0.1

Lastly, our experimental cell morphology results were obtained using SEM images of cryogenically fractured plaques along the centerline of the specimen. To ensure our simulated cell morphology aligned with experimental results, we placed probes and clipped them along the centerline of our simulated plaque sample. The clipping and probing functions help analyze the cell size and cell density along the center region, as shown in the figure below. Three probe locations (Figure 8b) were selected, and the cell morphology results were averaged and compared with experimental results.

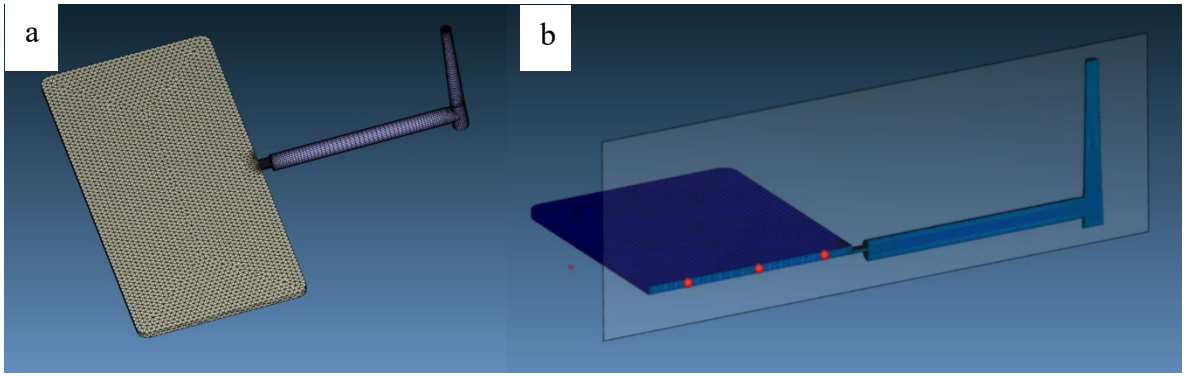

Figure 8 a) Meshed model of the plaque b) Probe locations chosen to match experimental results.

Figure 9 shows very good correlation between simulation and experimental results in terms of part density, cell size, cell density which validates the process and microstructure prediction capabilities of the DLC pathway.

Accepted Manuscript
Version of Record at: https://doi.org/10.1002/pen.26700

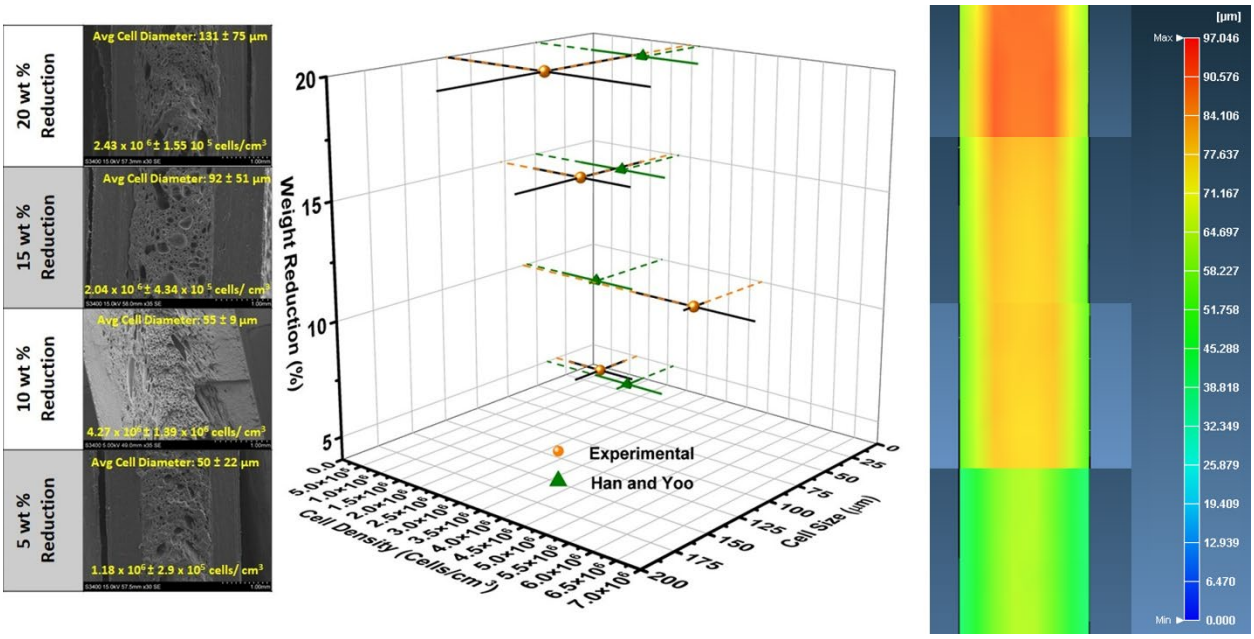

Figure 9. Comparison between experimental vs simulation prediction for cell size and cell density

Mechanical Material Model and Porosity Mapping from Process Simulations

Digimat was used to generate a material model to evaluate the mechanical behavior of the TPO dependent on the local porosity volume fraction. This approach is based around mean-field homogenization, a semi-analytical homogenization approach used to compute thermal and mechanical properties of multi-constituent materials like the current TPO foam. Once generated, the material model can compute/calculate the TPO mechanical properties for different porosity content.

A key step in this pathway is coupling porosity mapping from process simulation to the mechanical modeling approach. To enable that connection, another important step required is to transfer the porosity size and density from the Moldex 3D simulation mesh (donor mesh) onto the finite element analysis mesh (receiving mesh) to enable the material model to use that information determine the local element's mechanical properties and behavior. This mapping procedure uses Digimat through a "Integration point / Node to Node / Integration point" transfer algorithm defined in the Digimat user's manual [43]. Two key characteristics of the mapping procedure are:

1. The porosity data is mapped onto the FEA integration points (not the nodes)
2. Digimat converted porosity size and density into volume fraction during the mapping procedure to ensure the connection to the material model.

The first characteristic enables a strong coupling between the FEA strain computation and Digimat stiffness matrix computation using the porosity volume fraction provided. The second characteristic simplifies the connection between the data from Moldex 3D and the FEA model using only 1 variable instead of 2.

Accepted Manuscript
Version of Record at: https://doi.org/10.1002/pen.26700

FEA Model for Tensile and Flex Load Cases

Marc solver was used to simulate the 3-point bending and tensile tests performed on TPO specimens. The loading on the tensile model was applied through a node and a non-restrictive rigid body connection. The reason for this specific loading application was to simplify the post-processing. A fixed-displacement boundary condition was applied to the opposite surface to represent the tensile machine grips. The bending model was built using 20-node isoparametric hexahedral elements to help avoid shear locking during the sample bending. The same element type was used for the tensile test simulation model to minimize the differences in the simulation parameters between the two models and leave the differences to the boundary and loading conditions. Local seeding was used to ensure the presence of 6 elements through the sample thickness to ensure accurate porosity volume fraction distribution. The loading on the bending model is applied through a rigid surface, while the support is modeled as 2 surfaces spaced evenly on each side of the specimen Figure 10a. No friction was applied in the contact definition between the surfaces and the specimen, and the only boundary conditions used were to ensure the initial static equilibrium before initial loading. The material behavior was defined by coupling with the Digimat material model using the porosity volume fraction at each integration point [43]. The experimental inputs for process data card generation outlined in the material section serve as inputs for semi-empirical models used by the injection molding simulation solver to predict the melt flow behavior. Solid viscoelastic, PVT, crystallinity, and mechanical behavior are generally necessary for warpage prediction. The crystallization kinetics data can predict the degree of crystallinity during various cooling histories. The fluid viscoelasticity is useful for predicting flow-induced residual stress, die swell, and jet buckling.

One of the challenges in accurately modeling the behavior of the current process is the non-uniform microstructure over the thickness of the different testing specimens. The cross-section images of the porosity distribution over the thickness show that most of the voids are distributed in the core section of the specimen, which implicates a non-uniform mechanical behavior through the thickness (see Figure 4). The proposed digital lifecycle approach links the predicted porosity directly to the local material behavior through the calibrated material model, providing a more accurate material behavior definition through the thickness, as shown in Figure 10b.

a

Accepted Manuscript
Version of Record at: https://doi.org/10.1002/pen.26700

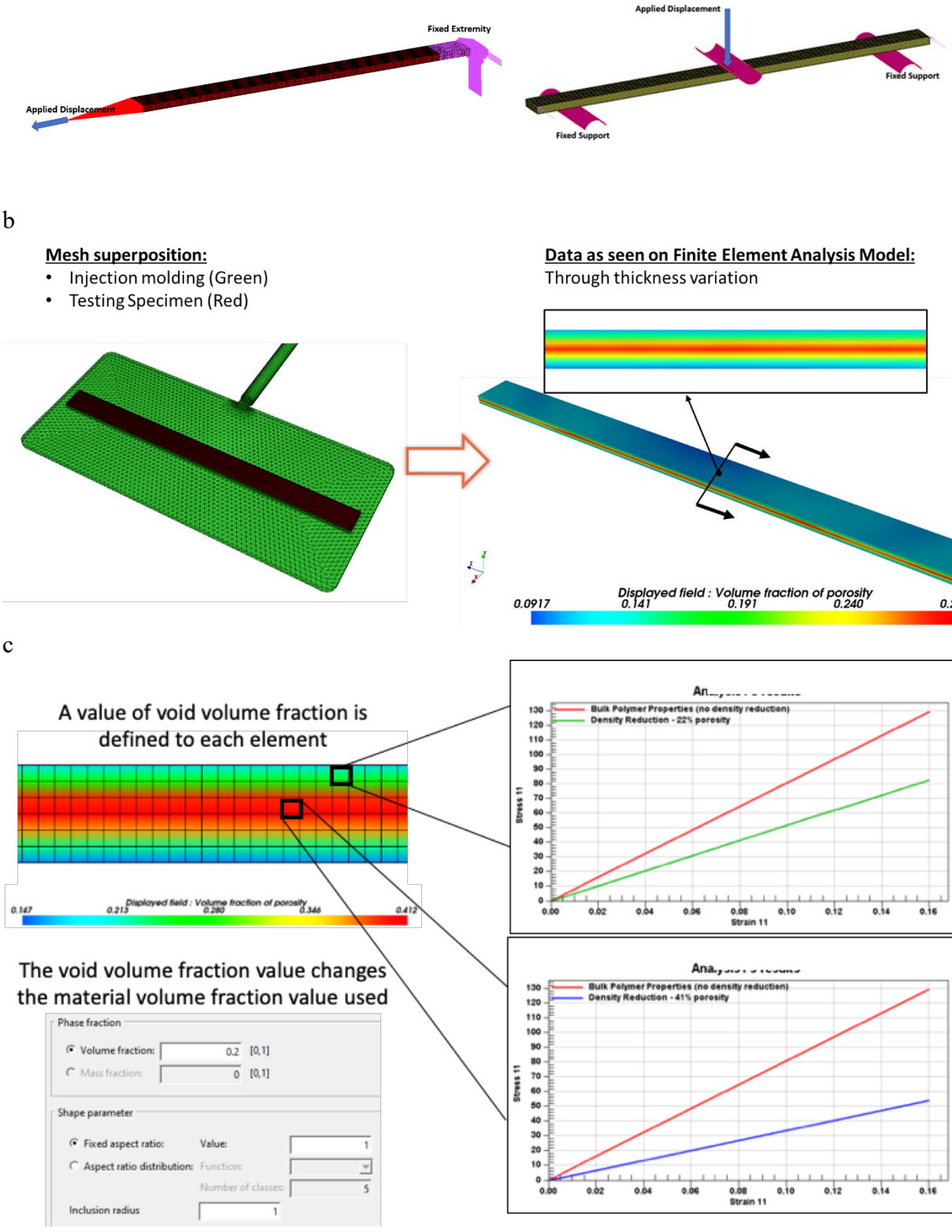

Figure 10. (a) Tensile and Flex FEA model (b) Transfer of Porosity Content Between Models. (b) DLC Pathway accounting for the non-uniform density distribution

This circumvents the need for experimental inputs from SEM images, such as measured core thickness and skin thickness of the injection molded foam, that are necessary with most theoretical

Accepted Manuscript
Version of Record at: https://doi.org/10.1002/pen.26700

or analytical models, unlike our DLC Pathway (Figure 10 c). Furthermore, the analytical models assume a uniform density distribution within the core, which is not the case, as seen in Figure 2, with process parameters significantly affecting the cell size, cell distribution, and density distribution at a microstructure level. This approximation can result in overprediction or underprediction of mechanical properties. The workflow also mitigates the need for experiments and relies only on simulation results for the through-the-thickness porosity content definition. Several analytical models have been proposed to determine the Young's Modulus [36], and Compressive modulus [44] using the physical microstructure morphology of the foam. Some of them relevant to this study are as shown below:

Kerner Model for normalized specific Youngs Modulus (E_{ST}):

$$\frac{E_{ST}}{E_P} = \frac{2[\rho_c(13 - 2\upsilon - 15\upsilon^2 + 5\alpha\upsilon\ - 7\alpha\ ) + (15\upsilon^2 + 12\upsilon - 27)]}{(\rho_c\alpha + 2)[\rho_c(13 - 2\upsilon - 15\upsilon^2) + (15\upsilon^2 + 12\upsilon - 27)]} \quad (8)$$

Ogorkiewicz and Sayigh model for normalized specific Youngs modulus (E_{ST}):

$$\frac{E_{ST}}{E_P} = \frac{\left[(\alpha + 2)\rho_c + \ (1 - \rho_c)^{(2/3)} - \ (1 - \rho_c)^{(1/3)}\right] + 2\ (1 - \rho_c)}{(\rho_c\alpha + 2)[1 - (1 - \rho_c)^{(1/3)} + (1 - \rho_c)^{(2/3)}]} \quad (9)$$

Lee and Westmann model for normalized specific Youngs modulus (E_{ST}):

$$\frac{\boldsymbol{E_{ST}}}{\boldsymbol{E_P}} = \frac{\boldsymbol{2[(\alpha - 3\upsilon - 3)\rho_c + 5 + 3\upsilon]}}{\boldsymbol{(\rho_c\alpha + 2)[5 + 3\upsilon - 3(1 + \upsilon)\rho_c]}} \quad (10)$$

Square Power-Law Model for normalized specific Youngs modulus (E_{ST}):

$$\frac{\boldsymbol{E_{SF}}}{\boldsymbol{E_P}} = \frac{\boldsymbol{\alpha^3\rho_c^2 + 2}}{\boldsymbol{(\rho_c\alpha + 2)}} \quad (11)$$

A = $2(3\alpha^2 + 6\ \alpha + 4)$
ρ_c = Mass density ratio i.e. foam relative density or volume fraction of its solid phase with respect to the cavity volume
υ = Poisson's ratio of unfoamed polymer / thermoplastic blend
α = core-to-skin thickness ratio of achieved foam

Table 5.Comparison of Experimental vs Analytical models vs Simulation Prediction for Youngs Modulus

Accepted Manuscript
Version of Record at: https://doi.org/10.1002/pen.26700

Lightweight %	Youngs Modulus [MPa] Experimental	Kerner [MPa]	Ogorkiewicz and Sayigh [MPa]	Square Power Law [MPa]	DLC Pathway - Simulation Results [MPa]
5%	648.7	685.81	707.93	671.17	683.63
10%	618.13	662.43	666.33	616.87	645.86
15%	535.12	640.60	653.45	602.03	598.6
20%	514.67	620.16	616.38	555.46	549.49
Avg Absolute Error		13.27 %	14.70%	6.02%	**7.12%**

Similarly for Flex modulus Mohyeddin et al. [34] highlighted two models that were of particular interest: Lee and Westmann model [35] and Ogorkiewicz and Sayigh model [36] are listed below.

Kerner Model for normalized specific Flex Modulus (E_{ST}):

$$\frac{E_{SF}}{E_P} = \frac{[\rho_c(A(15\upsilon^2 + 2\upsilon - 13) + 2\alpha^3(7 - 5\upsilon)) - A(15\upsilon^2 + 12\upsilon - 27)]}{(\rho_c\alpha + 2)(\alpha + 2)^2[\rho_c(-13 + 2\upsilon + 15\upsilon^2) - 15\upsilon^2 - 12\upsilon + 27)]} \quad (12)$$

Ogorkiewicz and Sayigh model for normalized specific flexural modulus (E_{SF}):

$$\frac{E_{SF}}{E_P} = \frac{\left[(1-\rho_c)^{(2/3)} - (1-\rho_c)^{(1/3)}\right](\alpha^3 - A) + \rho_c\alpha^3 + A}{(\rho_c\alpha + 2)(\alpha + 2)^2[1 - (1-\rho_c)^{(1/3)} + (1-\rho_c)^{(2/3)}]} \quad (13)$$

Lee and Westmann model:

$$\frac{E_{SF}}{E_P} = \frac{[3(1+\upsilon)(A - 2\alpha^3)]\rho_c - (5 + 3\upsilon)A}{3(\rho_c\alpha + 2)(\alpha + 2)^2[(1 + \upsilon)(\rho_c - 5 - 3\upsilon)]} \quad (14)$$

Square Power-Law Model:

$$\boldsymbol{\frac{E_{SF}}{E_P} = \frac{\alpha^3\rho_c^2 + A}{(\rho_c\alpha + 2)(\alpha + 2)^2}} \quad (15)$$

$A = 2(3\alpha^2 + 6\,\alpha + 4)$
ρ_c = Mass density ratio i.e., foam relative density or volume fraction of its solid phase with respect to the cavity volume
υ = Poisson's ratio of unfoamed polymer / thermoplastic blend
α = core-to-skin thickness ratio of achieved foam

Accepted Manuscript
Version of Record at: https://doi.org/10.1002/pen.26700

Table 6. Comparison of Experimental vs. Analytical models vs. Simulation Prediction for Flex Modulus

Lightweight %	Flex Modulus [MPa] Experimental	Kerner [MPa]	Ogorkiewicz and Sayigh [MPa]	Square Power Law [MPa]	DLC Pathway - Simulation Results [MPa]
5%	728.66	732.75	589.86	730.09	719.54
10%	622.83	494.97	505.51	489.35	660.24
15%	562.75	530.45	539.06	524.76	604.64
20%	583.21	474.05	495.19	465.29	570.70
Avg Absolute Error		11.39 %	14.30 %	12.15 %	**4.21 %**

A comparison has been made between the mechanical properties predicted using various analytical models in the literature and the simulated predictions obtained using the DLC pathway. This comparison, as shown in Table 5 and Table 6 confirms the DLC pathway predicting the least error across different lightweighting and analytical models. Although the Square power law did show comparable results for Young's modulus, it failed to capture the correct trend in terms of property retention and, more importantly, performed worse in terms of predicting the flexural modulus. Figure 11 shows a visual representation of the correlation between analytical models vs. DLC results with experimental results in terms of tensile and flexural modulus.

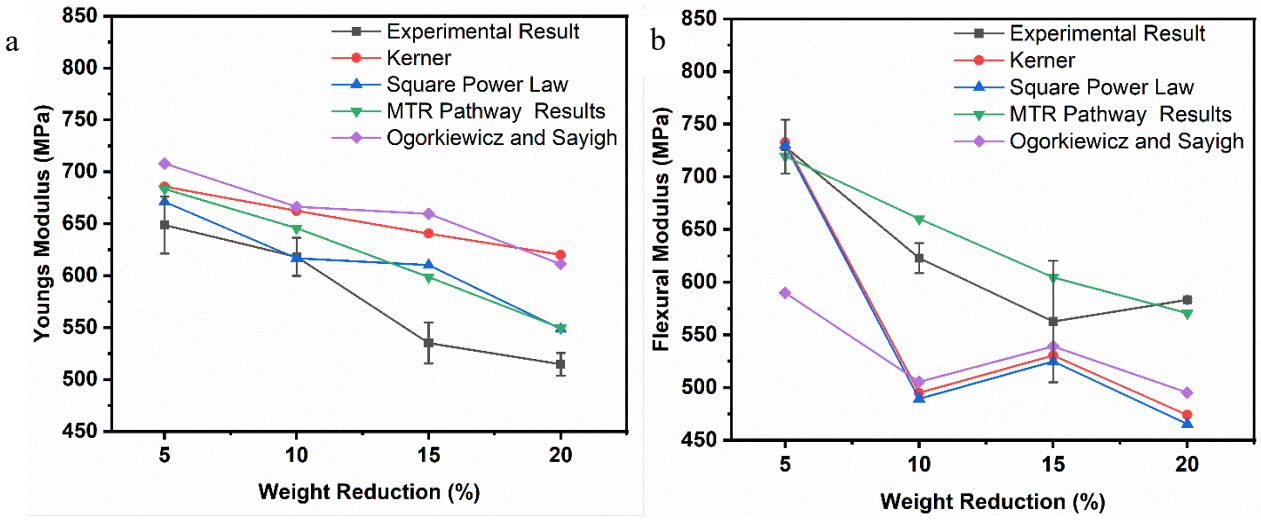

Figure 11. a)Comparison between experimental vs simulation prediction for Youngs Modulus. b) Comparison between experimental vs simulation prediction for Flex Modulus

Though there are multiple homogenization methods [45] for the property evaluation of materials, many of those models are developed for applications at a microstructure level, which is not a good representation of the variable microstructures found on larger structures or parts. As porous materials can be compared to composites, some of the constitutive models used to evaluate the mechanical response of porous materials adapt to the mean-field Eshelby-based homogenization method. Ramaskrishnan-Arunachalam, Generalized Self-Consistent Method (GSCM),

Accepted Manuscript
Version of Record at: https://doi.org/10.1002/pen.26700

Differential Method (DM), Composite Spherical Model (CSM), and Mori-Tanaka are compared in [46] against more accurate finite element-based methods (Direct Models). In this regard, the Digital Lifecycle pathway presented in this study is a hybrid of direct representative modeling approaches, homogenization, and finite element approaches. This allows us to circumvent many of the simplifying assumptions used in the direct representative models, the need for exhaustive experimental data for modeling technique-based approaches where inputs are calibrated using experimental microstructure data and constitutive models such as phenomenological models that also require significant experimental data and homogenization-based models that do not capture microstructure variation within complex part geometries [22]. The advantages of the DLC approach over these modeling approaches are illustrated in Figure 12.

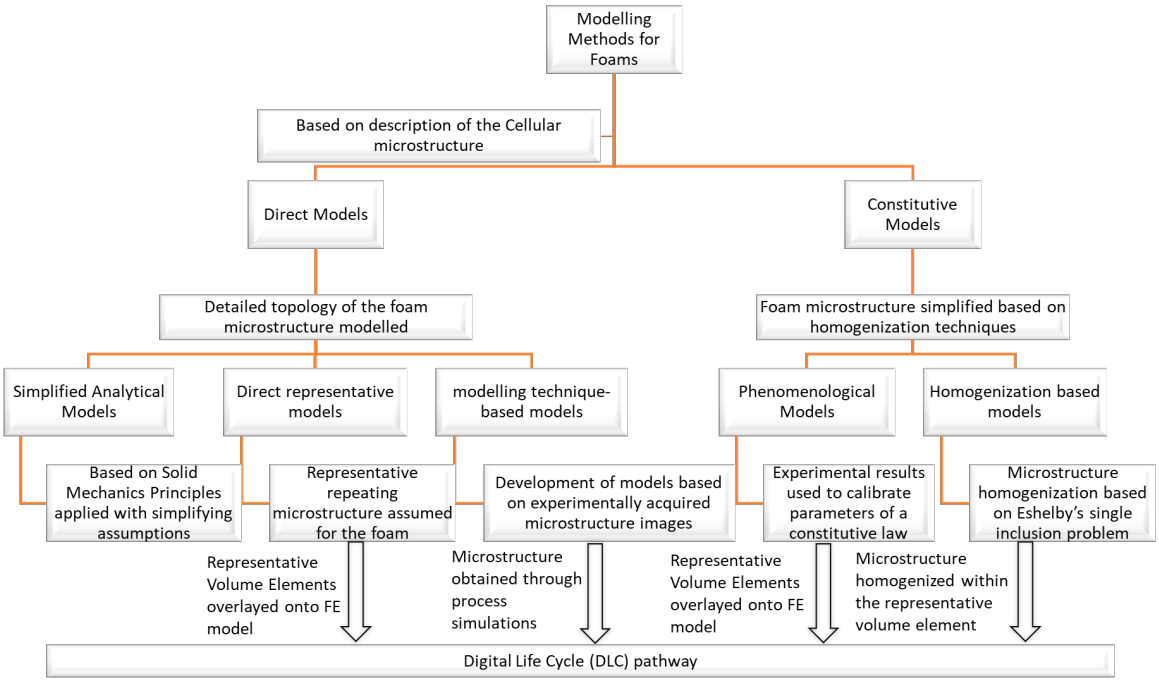

Figure 12: Modelling attributes incorporated into DLC Pathway

Conclusion

This study aimed to develop a sustainable foam injection molding process to manufacture microcellular foams of TPO blends supplied by OEM. Through process optimization, samples with up to 10% density reductions were achieved while maintaining acceptable mechanical property retention, including tensile, flexural, and instrumented impact. Furthermore, the samples demonstrated good paint adhesion performance, as evidenced by their minimal color difference and gloss retention. The study also revealed that differences in microcellular cell morphology were closely linked to property retention in mechanical, appearance, and thermal benchmarks. To this end, a material-process-microstructure-performance (MP2) relationships was established to understand better the role of microcellular cell morphology in determining the properties of the TPO foam. Furthermore, the study created a Digital Lifecycle pathway by developing a rheological

data card for process simulations. This approach enabled the identification of appropriate nucleation and bubble growth models to predict foam microstructure. Finally, the predicted microstructure was mapped on an FEA mesh to predict tensile and flexural modulus accurately. The DLC pathway allows for complex microstructures, with multiple inclusions, fillers, and blends, to be obtained through process simulations. Currently, incorporating fillers, fibers, and other additives requires significant experimental results to be generated before any analytical model can be developed. Furthermore, the nature of the additives, fillers, and reinforcements affect the specificity of these analytical models [22,47]. These microstructures can be overlaid using finite element software onto complex macro-scale part geometries to determine their mechanical performance. Overall, this study demonstrates the potential of a sustainable foam injection molding process to manufacture TPO foam with acceptable mechanical and paint adhesion properties. It also highlights the importance of considering microcellular cell morphology in determining the properties of TPO foam and the usefulness of a Digital Lifecycle pathway in predicting foam microstructure and mechanical properties.

Acknowledgements

This work was supported as part of the AIM for Composites, an Energy Frontier Research Center funded by the U.S. Department of Energy, Office of Science, Basic Energy Sciences at the University of Delaware under award #DE-SC0023389. Additionally, the authors would like to acknowledge Tim Haake for the use of capillary rheometers at the Polymers Center for Excellence.

References

1. Park, C.-K.; Kan, C.-D. (Steve); Hollowell, W.T.; Hill, S.I.; George Washington University, A.; LLC, W.T.H.C.; Dayton, U. of; Administration, N.H.T.S. Investigation of Opportunities for Lightweight Vehicles Using Advanced Plastics and Composites. *Natl. Highw. Traffic Saf. Adm.* **2012**, 416p.
2. Pradeep, S.A.; Iyer, R.K.; Kazan, H.; Pilla, S. Automotive Applications of Plastics: Past, Present and Future. In *Applied Plastics Engineering Handbook: Processing, Materials, and Applications*; Kutz, M., Ed.; Elsevier: Oxford, 2017; pp. 651–674 ISBN 9780323266987.
3. Chu, J.; Xiang, C.; Sue, H.J.; Hollis, R.D. Scratch Resistance of Mineral-Filled Polypropylene Materials. *Polym. Eng. Sci.* **2000**, *40*, 944–955, doi:10.1002/pen.11222.
4. Mehta, S.; Mirabella, F.M.; Rufener, K.; Bafna, A. Thermoplastic Olefin / Clay Nanocomposites : Morphology and Mechanical Properties. *J. Appl. Polym. Sci.* **2004**, 928–936.
5. Iyigundogdu, Z.; Basar, B.; Couvreur, R.; Tamrakar, S.; Yoon, J.; Ersoy, O.G.; Sahin, F.; Mielewski, D.; Kiziltas, A. Thermoplastic Elastomers Containing Antimicrobial and Antiviral Additives for Mobility Applications. *Compos. Part B* **2022**, *242*, 110060, doi:10.1016/j.compositesb.2022.110060.
6. Jing, X.; Li, Y.; Zhu, J.; Chang, L.; Maganti, S.; Naik, N.; Xu, B. Bin; Murugadoss, V.; Huang, M.; Guo, Z. Improving Thermal Conductivity of Polyethylene/Polypropylene by Styrene-Ethylene-Propylene-Styrene Wrapping Hexagonal Boron Nitride at the Phase Interface. *Adv. Compos. Hybrid Mater.* **2022**, *5*, 1090–1099, doi:10.1007/s42114-022-00438-x.

7. Pradeep, S.A.; Shukla, S.; Brown, N.; Pilla, S. Thermoplastics Foams : An Automotive Perspective. In *Lightweight and Sustainable Materials for Automotive Applications*; CRC Press, Taylor & Francis Group, 2017; pp. 369–400 ISBN 9781315152967.
8. Shirvanimoghaddam, K.; Balaji, K. V; Yadav, R.; Zabihi, O.; Ahmadi, M.; Adetunji, P.; Naebe, M. Balancing the Toughness and Strength in Polypropylene Composites. *Compos. Part B* **2021**, *223*, 109121, doi:10.1016/j.compositesb.2021.109121.
9. Coste, G.; Negrell, C.; Caillol, S. From Gas Release to Foam Synthesis, the Second Breath of Blowing Agents. *Eur. Polym. J.* **2020**, *140*, 110029, doi:10.1016/j.eurpolymj.2020.110029.
10. Kharbas, H.A.; McNulty, J.D.; Ellingham, T.; Thompson, C.; Manitiu, M.; Scholz, G.; Turng, L.S. Comparative Study of Chemical and Physical Foaming Methods for Injection-Molded Thermoplastic Polyurethane. *J. Cell. Plast.* **2017**, *53*, 373–388, doi:10.1177/0021955X16652107.
11. Guo, M.C.; Santoni, A.; Heuzey, M.C.; Carreau, P.J. Occurrence of Surface Defects in TPO Injected Foam Parts. *J. Cell. Plast.* **2007**, *43*, 273–296, doi:10.1177/0021955X07077191.
12. Santoni, A.; Guo, M.C.; Heuzey, M.C.; Carreau, P.J. Surface Defects of TPO Injected Foam Parts for Automotive Applications. *Int. Polym. Process.* **2007**, *22*, 204–212, doi:10.3139/217.2004.
13. Peyda, S.; Morshedian, J.; Karbalaei-Bagher, M.; Baharvand, H.; Khorasani, M.T. A Novel Technique in the Foaming Process of EPDM/PP: Via Microwave Radiation: The Effect of Blend Compatibilization and Additive Encapsulation. *RSC Adv.* **2016**, *6*, 81400–81407, doi:10.1039/c6ra14211g.
14. Hyde, L.J.; Kishbaugh, L.A.; Katterman, J.A. How Microcellular Foam Molding Changes the Cost Structure of Injection Molded Automotive Components: A Review of the Process and Automotive Applications. *SAE Trans. J. Mater. Manuf.* **2003**, *111*, 463–474, doi:10.4271/2002-01-0717.
15. Li, G.; Gunkel, F.; Wang, J.; Park, C.B.; Altstädt, V. Solubility Measurements of N2 and CO2 in Polypropylene and Ethene/Octene Copolymer. *J. Appl. Polym. Sci.* **2007**, *103*, 2945–2953, doi:10.1002/app.25163.
16. Wong, S.; Lee, J.W.S.; Naguib, H.E.; Park, C.B. Effect of Processing Parameters on the Mechanical Properties of Injection Molded Thermoplastic Polyolefin (TPO) Cellular Foams. *Macromol. Mater. Eng.* **2008**, *293*, 605–613, doi:10.1002/mame.200700362.
17. Kim, S.G.; Lee, J.W.S.; Park, C.B.; Sain, M. Enhancing Cell Nucleation of Thermoplastic Polyolefin Foam Blown with Nitrogen. *J. Appl. Polym. Sci.* **2010**, *118*, 1691–1703, doi:10.1002/app.32294.
18. Kim, S.G.; Leung, S.N.; Park, C.B.; Sain, M. The Effect of Dispersed Elastomer Particle Size on Heterogeneous Nucleation of TPO with N2 Foaming. *Chem. Eng. Sci.* **2011**, *66*, 3675–3686, doi:10.1016/j.ces.2011.05.003.
19. Xi, Z.; Chen, J.; Liu, T.; Zhao, L.; Turng, L.S. Experiment and Simulation of Foaming Injection Molding of Polypropylene/Nano-Calcium Carbonate Composites by Supercritical Carbon Dioxide. *Chinese J. Chem. Eng.* **2016**, *24*, 180–189, doi:10.1016/j.cjche.2015.11.016.
20. Oikonomou, D. Analysis and Validation of Varied Simulation Parameters in the Context of Thermoplastic Foams and Special Injection Molding Processes. **2023**.
21. Hössinger-Kalteis, A.; Reiter, M.; Jerabek, M.; Major, Z. Overview and Comparison of Modelling Methods for Foams. *J. Cell. Plast.* **2020**, doi:10.1177/0021955X20966329.

22. Shaayegan, V.; Ameli, A.; Wang, S.; Park, C.B. Experimental Observation and Modeling of Fiber Rotation and Translation during Foam Injection Molding of Polymer Composites. *Compos. Part A* **2016**, *88*, 67–74, doi:10.1016/j.compositesa.2016.05.013.
23. Daniel, I.M.; Cho, J.; Werner, B.T. Characterization and Modeling of Stain-Rate-Dependent Behavior of Polymeric Foams. *Compos. PART A* **2013**, *45*, 70–78, doi:10.1016/j.compositesa.2012.10.003.
24. Wanchoo, P.; Kishore, S.; Shukla, A. Hydrostatic High Strain Rate Loading Response of Closed-Cell Polymeric Foams as a Function of Mass Density. *Compos. Part B* **2022**, *247*, 110318, doi:10.1016/j.compositesb.2022.110318.
25. Pradeep, S.A.; Zheng, T.; Yerra, V.A.; Pilla, S. Automotive Lightweighting via Supercritical Foam Injection Molding of Thermoplastic Olefin. *Annu. Tech. Conf. - ANTEC, Conf. Proc.* **2019**, *2019-March*, 3–7.
26. Naguib, H.E.; Park, C.B.; Panzer, U.; Reichelt, N. Strategies for Achieving Ultra Low-Density Polypropylene Foams. *Polym. Eng. Sci.* **2002**, *42*, 1481–1492, doi:10.1002/pen.11045.
27. Lee, J.; Turng, L.-S.; Dougherty, E.; Gorton, P. A Novel Method for Improving the Surface Quality of Microcellular Injection Molded Parts. *Polymer (Guildf).* **2011**, *52*, 1436–1446, doi:10.1016/j.polymer.2011.01.026.
28. Xu, J. *Microcellular Injection Molding*; Wiley, 2010; ISBN 9780470466124.
29. Guanghong, H.; Yue, W. Microcellular Foam Injection Molding Process. **2012**, doi:10.5772/34513.
30. Ameli, A.; Jahani, D.; Nofar, M.; Jung, P.U.; Park, C.B. Development of High Void Fraction Polylactide Composite Foams Using Injection Molding: Mechanical and Thermal Insulation Properties. *Compos. Sci. Technol.* **2014**, *90*, 88–95, doi:10.1016/j.compscitech.2013.10.019.
31. Burns, T.D. Development and Application of a Reduced Thermal Expansion Polycarbonate/ABS Engineering Thermoplastic Blend for Automotive Exterior Body Panels. *SAE Tech. Pap.* **1991**, doi:10.4271/910436.
32. Sun, X.; Kharbas, H.; Peng, J.; Turng, L.-S. A Novel Method of Producing Lightweight Microcellular Injection Molded Parts with Improved Ductility and Toughness. *Polymer (Guildf).* **2015**, *56*, 102–110, doi:10.1016/j.polymer.2014.09.066.
33. Yang, Z.; Peng, H.; Wang, W.; Liu, T. Crystallization Behavior of Poly(ε-Caprolactone)/Layered Double Hydroxide Nanocomposites. *J. Appl. Polym. Sci.* **2010**, *116*, 2658–2667, doi:10.1002/app.
34. Mohyeddin, A. Theoretical Evaluation of Tensile and Flexural Moduli of Structural Polymer Foams. *J. Cell. Plast.* **2014**, *50*, 221–239, doi:10.1177/0021955X14524082.
35. Lee, J.; Westmann, R.A. Hollow-Sphere-Reinforced Composites. *J. Compos. Mater.* **1970**, *4*, 242–252.
36. Ogorkiewicz, R.M.; Sayigh, A.A.M. An Approximate Method of Predicting the Bending of Thermoplastic Beams. *Polymer (Guildf).* **1973**, *14*, 584–586, doi:10.1016/0032-3861(73)90144-4.
37. Kumar, V.; Juntunen, R.P.; Barlow, C. Impact Strength of High Relative Density Solid State Carbon Dioxide Blown Crystallizable Poly(Ethylene Terephthalate) Microcellular Foams. *Cell. Polym.* **2000**, *19*, 25–37.
38. Bureau, M.N.; Gendron, R. Mechanical–Morphology Relationship of PS Foams*. **2003**, doi:10.1177/002195503032452.

39. David E. Pierick;Jere R. Anderson; Sung W. Cha; Liqin Chen; James F. Stevenson, Morristown; Dana E. Laing, er, M. INJECTION MOLDING OF POLYMERIC MATERIAL 2005, *1*.
40. Li, S.; Zhao, G.; Wang, G.; Guan, Y.; Wang, X. Influence of Relative Low Gas Counter Pressure on Melt Foaming Behavior and Surface Quality of Molded Parts in Microcellular Injection Molding Process. *J. Cell. Plast.* **2014**, *50*, 415–435, doi:10.1177/0021955X14525961.
41. Cha, S.W.; Yoon, J.D. The Relationship of Mold Temperatures and Swirl Marks on the Surface of Microcellular Plastics. *Polym. - Plast. Technol. Eng.* **2005**, *44*, 795–803, doi:10.1081/PTE-200060811.
42. Taki, K. Experimental and Numerical Studies on the Effects of Pressure Release Rate on Number Density of Bubbles and Bubble Growth in a Polymeric Foaming Process. *Chem. Eng. Sci.* **2008**, *63*, 3643–3653, doi:10.1016/j.ces.2008.04.037.
43. MI, H. *Digimat: User Manual*; 2021;
44. Rahimidehgolan, F.; Altenhof, W. Compressive Behavior and Deformation Mechanisms of Rigid Polymeric Foams : A Review. *Compos. Part B* **2023**, *253*, 110513, doi:10.1016/j.compositesb.2023.110513.
45. Zhao, J.; Guo, C.; Zuo, X.; Román, A.J.; Nie, Y.; Su, D.X.; Turng, L.S.; Osswald, T.A.; Cheng, G.; Chen, W. Effective Mechanical Properties of Injection-Molded Short Fiber Reinforced PEEK Composites Using Periodic Homogenization. *Adv. Compos. Hybrid Mater.* **2022**, *5*, 2964–2976, doi:10.1007/s42114-022-00518-y.
46. El Ghezal, M.I.; Maalej, Y.; Doghri, I. Micromechanical Models for Porous and Cellular Materials in Linear Elasticity and Viscoelasticity. *Comput. Mater. Sci.* **2013**, *70*, 51–70, doi:10.1016/j.commatsci.2012.12.021.
47. Fei, Y.; Chen, F.; Fang, W.; Xu, L.; Ruan, S.; Liu, X.; Zhong, M.; Kuang, T. High-Strength , Flexible and Cycling-Stable Piezo-Resistive Polymeric Foams Derived from Thermoplastic Polyurethane and Multi-Wall Carbon Nanotubes. *Compos. Part B* **2020**, *199*, 108279, doi:10.1016/j.compositesb.2020.108279.